A quasi-objective single buoy approach for Lagrangian coherent structures and sea ice fracture events

Nikolas O. Aksamit[1, 2], Randall K. Scharien[1], and Jennifer K. Hutchings[3]

[1]Department of Geography, University of Victoria, Canada
[2]School of Earth and Environment, University of Canterbury, New Zealand
[3]College of Earth, Ocean, and Atmospheric Sciences, Oregon State University, USA

Correspondence: Nikolas O. Aksamit (naksamit@uvic.ca)

Abstract. Sea ice deformation and dynamics play a significant role in atmosphere-ice-ocean coupling. Deformation patterns in sea ice can be observed at a wide range of spatial scales, though high resolution objective quantification of these features remains difficult. In an effort to better understand local deformation of sea ice, we adapt the Trajectory Stretching Exponents (TSEs), quasi-objective measures of Lagrangian stretching in continuous media, to sea ice buoy data, and develop a temporal analysis of TSE time series. TSEs provide an approximation of Lagrangian coherent structure diagnostics when only sparse trajectory data is available. As TSEs do not require multiple buoys, we find they have an expanded range of use when compared with traditional Eulerian buoy-array deformation metrics, and provide local-stretching information below the length-scales possible when averaging over buoy-arrays. We verify the ability of TSEs to temporally and spatially identify dynamic fracture events for three different sea ice datasets, with buoys identifying fracture domains ranging tens to hundreds of kilometers in diameter.

1   Introduction

The Arctic is warming at a much greater rate than the rest of the Earth and sea ice plays an important role in regulating energy exchanges between the atmosphere, cryosphere, and ocean. The recent decline in sea ice extent and the prevalence of younger, thinner ice is well documented (Rothrock et al., 1999; Kwok and Rothrock, 2009) with thin ice being more susceptible to deformation and fracture. As the ice warms in spring, melt is accelerated around existing fractures, creating a positive feedback through reduction in albedo and the presence of more open water, leading to Arctic amplification (Serreze and Francis, 2006). Changes in the Arctic sea ice cover in recent years have also led to modifications of larger atmospheric circulation patterns (Moore et al., 2018), and mid-latitude weather (Siew et al., 2020). It is therefore of great importance to accurately represent sea ice dynamics to understand the state of ice deformation, fracture, and refreezing, as well as the impacts on global climate, infrastructure in Arctic waters, and access for northern communities.

Synoptic storms provide a link between large-scale and local-scale atmospheric forcing that directly influence the state of Arctic sea ice (Cohen et al., 2017). Recent studies have shown that even short winter storms can have long-term impacts on sea ice extent and melt (Graham et al., 2019b; Lukovich et al., 2021). Obtaining local or regional information on the state of sea-ice can thus give an indication of future sea ice melt rates and potential weather impacts. Synthetic aperture radar

25 (SAR) can provide high spatial resolution gridded measurements of sea ice motion and leads (e.g., Krumpen et al., 2021), but has limitations with respect to spatial and temporal sampling, errors in ice motions estimates, and computational burden. In contrast, buoy GPS trajectories are often sampled at much higher temporal resolution (hourly and sub-hourly timescales) and can provide a wealth of true sea ice motion data. Quantitative methods that identify coherent structures and deformation patterns in sea ice are thus critical for understanding atmosphere-ice-ocean exchange processes in many domains. As buoys passively

30 follow ice floes, and are typically sparse in the spatial domain, we have limited control over where the data will be available, and how buoy array shapes will change over time. Therefore, quantitative methods that can robustly identify important sea ice flow features (i.e. coherent structures), and how they change, from sparse buoy trajectories with ever-evolving buoy array geometries, could provide vital near-real time information on changing fracture dynamics in vital regions during the entire winter.

35 With this in mind, we approach understanding sea ice dynamics from a Lagrangian coherent structure (LCS) perspective, where separations between distinct LCS may correspond with strong shear zones or separation features, such as cracks and ridges. Resolving the time-varying dynamics of these coherent structures may also help identify periods of significant ice modification, such as influential storms or other breakup events. Previous efforts to identify sea ice deformation patterns with LCS utilized gridded sea ice displacement fields, but were hindered by artifacts from assimilating multiple velocity data-

40 streams, and the resolution of the velocity fields (Szanyi et al., 2016a, b). These mathematical methods relied on spatial gradients of the flow map, and thus required gridded velocity data.

As an alternative approach, we use novel single-buoy stretching diagnostics, the trajectory stretching exponents (TSEs) (Haller et al., 2021, 2022), to approximate the influence of specific LCS. For a trajectory $x(t)$, TSEs are quasi-objective Lagrangian metrics of material stretching. That is, they approximate true material stretching in slowly varying flows (i.e. when

45 Lagrangian time scales dominate Eulerian time scales, as is typical in geophysical flows). As shown by Haller et al. (2021), TSEs identify the same hyperbolic LCS as the widely-used finite-time Lyapunov exponent (FTLE) (Haller, 2015) in open ocean currents, and provide significant advantages when identifying structures in sparse, randomly-positioned trajectory data. As hyperbolic LCS detail regions of significant attraction, repulsion, and shear, we use TSEs to find regions and times when sea ice buoys are nearby hyperbolic LCS in the ice motion fields as a proxy for stretching, compression, or shear.

50 The present research shows TSEs identify local regions and periods of significant stretching and compression with much larger influence, some of which is not evident with conventional metrics. We verify the presence of these coherent stretching and compression features with concurrent lead formation in remotely-sensed data, and synoptic storm analysis. We discuss several logistical, and computational advantages with the single-buoy diagnostics, as well as future insights possible with TSE applications. We also compare our LCS based method of spatio-temporal ice fracture analysis with standard Eulerian

55 array-based rate of strain metrics.

2 Methods and Material

For a continuously differentiable velocity field $\mathbf{v}(\mathbf{x},t)$, a particle's trajectory $\boldsymbol{x}(t)$ is governed by the equation $\dot{\boldsymbol{x}}(t) = \mathbf{v}(\boldsymbol{x},t)$, where t is the time variable. Consider a material curve $\boldsymbol{\gamma}(t;s) \subset U \subset \mathbb{R}^2$, parameterized by the scalar parameter $s \in \mathbb{R}$ at time t, that has evolved from the initial curve $\boldsymbol{\gamma}(t_0;s)$. One can quantify the stretching of vectors tangent to this material curve using the equation of variations. In a steady flow, particle trajectories are material curves, and the Lagrangian velocity vector $\boldsymbol{v}(t)$ evolve as material tangent vectors following

$$\dot{\boldsymbol{v}}(t) = \nabla\mathbf{v}(\boldsymbol{x}(t),t)\boldsymbol{v}. \tag{1}$$

Haller et al. (2021) showed the the average material stretching, and averaged hyperbolicity strength over the time interval $t \in [t_0, t_N]$ of the initial material tangent vector (Lagrangian velocity) $\boldsymbol{v}_0 = \mathbf{v}(\boldsymbol{x}_0)$ can be written as

$$\lambda_{t_0}^{t_N}(\boldsymbol{x}_0, \boldsymbol{v}_0) = \frac{1}{t_N - t_0} \log \frac{|\mathbf{v}(\boldsymbol{x}(t_N))|}{|\boldsymbol{v}_0|} \tag{2}$$

$$\bar{\lambda}_{t_0}^{t_N}(\boldsymbol{x}_0, \boldsymbol{v}_0) = \frac{1}{t_N - t_0} \int\limits_{t_0}^{t_N} \left| \frac{d}{dt} \log \frac{|\mathbf{v}(\boldsymbol{x}(t))|}{|\boldsymbol{v}_0|} \right| dt. \tag{3}$$

Note, in an unsteady flow, the right hand side of Eq (1) would also include a $\delta_t \mathbf{v}(\boldsymbol{x}(t),t)$ term. For unsteady flows, the magnitude of the approximation error of tangential stretching in Eq (2) strongly depends on the slowly-varying nature of the flow (small $\delta_t \mathbf{v}(\boldsymbol{x}(t),t)$). Sea ice velocities are verified to generate a pointwise slowly-varying flow field in Appendix A1 using Polar Pathfinder Daily 25 km EASE-Grid Sea Ice Motion Vectors (Tschudi et al., 2018), similar to the analysis for ocean currents by Haller et al. (2022). Our validation of the slowly-varying assumption does not depend on a specific integration time, but does rely heavily on the temporal and spatial resolution of the underlying Pathfinder velocity field.

Furthermore, this material stretching assumes the trajectory is traveling in a continuous, incompressible material. While it is true that sea ice velocity fields are not continuously differentiable, they are piecewise continuously differentiable (between fractures), and thus trajectory stretching exponents are well-defined in sections of continuously deforming media. That is, if ice fractures do not form exactly at a buoy's location. In a steady incompressible two-dimensional flow, a negative stretching exponent, $\lambda_{t_0}^{t_N}$, equals the growth exponent of a vector normal to the material line formed by the trajectory $\mathbf{x}(t)$ (Haller et al., 2021). For unsteady compressible flows, such as sea ice, $\lambda_{t_0}^{t_N}$ and $\bar{\lambda}_{t_0}^{t_N}$ are proxies for the material change in a plane normal to the trajectory, including stretching, ridging, and fracture. Negative $\lambda_{t_0}^{t_N}$ values indicate compression, and positive values indicate stretching along the trajectory. The degree to which this differs from the growth exponent of that plane depends on slowly-varying and compressibility conditions. With these consideration in mind, we focus on mid-winter and early spring ice dynamics prior to minimize extensive fracturing of the ice cover.

For discrete observational trajectory data with an initial position $\mathbf{x}_0 = \mathbf{x}(0)$, we can adapt Eqs (2) and (3) following Haller et al. (2021), and define the trajectory stretching exponents

85 $$\text{TSE}_{t_0}^{t_N}(\mathbf{x}_0) = \frac{1}{t_N - t_0} \log \frac{|\dot{\mathbf{x}}(t_N)|}{|\dot{\mathbf{x}}(t_0)|} \tag{4}$$

$$\overline{\text{TSE}}_{t_0}^{t_N}(\mathbf{x}_0) = \frac{1}{t_N - t_0} \sum_{i=0}^{N-1} \left| \log \frac{|\dot{\mathbf{x}}(t_{i+1})|}{|\dot{\mathbf{x}}(t_i)|} \right|. \tag{5}$$

where TSE is the measure of trajectory stretching or contraction, and $\overline{\text{TSE}}$ is the measure of hyperbolicity strength (Haller et al., 2021) for discrete data. The summand in eq. (5) is strictly positive, and thus $\overline{\text{TSE}}$ measures the cumulative stretching and contraction. In contrast to eqs. (7 - 9), TSEs do not differentiate between contributions from divergence or shear to the

90 stretching of a material. Rather, they identify the stretching in the direction of vectors tangent to the trajectory. TSE and $\overline{\text{TSE}}$ have been shown to accurately separate dynamically distinct regions (eddies and fronts) in sparsely-sampled open ocean flows. We extend this to the exceptionally sparse sea ice domain by developing a temporal analysis of stretching exponent time series.

For slowly-varying (steady) flows, TSE approximates (equals) the finite-time Lyapunov exponent associated with the initial vector $\dot{\mathbf{x}}_0$ at the initial position $\mathbf{x}_0$, an objective Lagrangian measure of deformation over time (Ott and Yorke, 2008; Haller

95 et al., 2021). The difference between the average stretching measured by TSE and stretching in the plane orthogonal to the initial vector v_0 is a function of the rheology of ice and the magnitude of δ_t, the temporal derivative of sea ice velocities along the trajectory. The slowly-varying of sea ice is evaluated in Appendix A1.

There are limited frame-indifferent Lagrangian alternatives for coherent structure identification with sparse buoy data to compare to. One notable exception is single-point (squared) relative dispersion (Haller and Yuan, 2000), with similar variations

100 applied in various contexts by Rampal et al. (2009), Lukovich et al. (2014), and Lukovich et al. (2015). One cannot, however, generate both spatial patterns and time series in a manner comparable to TSE as relative dispersion relies on initially nearby buoys whose motions decorrelate at longer time scales. Relative dispersion shows spatially coherent structures for a short window of time, but as the initially close buoys become decorrelated, one must reselect new buoy pairs, thus preventing a single meaningful time-series of local conditions. In this way it is more often used for understanding scaling relationships of

105 dispersion.

One common buoy-based approach for temporally-resolving horizontal sea ice deformation is to approximate the average divergence and shear inside a polygon whose vertices are buoys, using a discretized contour integral (Green's theorem) approach at each timestep. This approach can be traced back to at least the early 1990's where it was applied to sea ice motion fields from sequential SAR frames (Kwok et al., 1990). For buoys, deformation metrics can be calculated by tracking pre-defined

110 polygons (Hutchings et al., 2011, 2012), or by looking at statistics for all suitable triangles (e.g. no small angles) in an array (Itkin et al., 2017). The components of the 2D rate of strain tensor are then approximated as follows:

$$\frac{\partial u}{\partial x} = \frac{1}{2A} \sum_{i=1}^{N} (u_{i+1} + u_i)(y_{i+1} - y_i),$$

$$\frac{\partial u}{\partial y} = -\frac{1}{2A} \sum_{i=1}^{N} (u_{i+1} + u_i)(x_{i+1} - x_i),$$

$$\frac{\partial v}{\partial x} = \frac{1}{2A} \sum_{i=1}^{N} (v_{i+1} + v_i)(y_{i+1} - y_i),$$

115
$$\frac{\partial v}{\partial y} = -\frac{1}{2A} \sum_{i=1}^{N} (v_{i+1} + v_i)(x_{i+1} - x_i)$$

(6)

where i is a counterclockwise index of the N vertices of the polygon of interest, and A is the area of the polygon. The maximum rate of shear (shr), divergence (div), and total deformation (D) are then calculated as

$$\text{shr} = \sqrt{\left(\frac{\partial u}{\partial x} - \frac{\partial v}{\partial y}\right)^2 + \left(\frac{\partial u}{\partial y} + \frac{\partial v}{\partial x}\right)^2}, \tag{7}$$

120
$$\text{div} = \frac{\partial u}{\partial x} + \frac{\partial v}{\partial y}. \tag{8}$$

$$D = \sqrt{\text{div}^2 + \text{shr}^2} \tag{9}$$

While these Eulerian strain-based metrics provide an imperfect comparison to an LCS-based approach to ice deformation, they are commonly used in sea ice dynamics research, and can generate long time series for suitably chosen polygons. Notable complications with the Green's theorem method includes sensitivities to user discretion, accounting for GPS signal-to-noise ratios, and several physical inaccuracies arising from discretization. As arrays of buoys passively follow ice floes, they typically do not maintain a shape that allows accurate calculation of the spatial velocity gradients from drift trajectories. Some of these issues have been previously discussed by Lindsay and Stern (2003); Hutchings et al. (2012); Dierking et al. (2020), including the polygon array selection method. Because of the necessary discretization of a continuous boundary, integral approximations by finite sums in the Green's theorem approach can also generate errors. Lindsay and Stern (2003) mentions boundary representation errors for nonlinear velocity fields, but only errors from discontinuities (cracks) that intersect polygon boundaries have been quantified (e.g., Lindsay and Stern, 2003). Uncertainty also stems from the trapezoid rule approximation of the contour integral. For a known continuous velocity field (e.g. without cracks), the upper bound of integral approximations can be quantified (e.g., Atkinson, 1989,), though an explicit impact of this error cannot be found in the sea ice literature.

As is detailed in Appendix A2, the trapezoid rule error can cause equilateral triads to indicate both divergent and convergent
135   conditions in a steady, continuous (crack-free), divergence-free flow, depending on orientation.

In light of these complications, alternative methods that do not rely on buoy geometry or orientation, such as single trajectory
metrics, could be largely beneficial, even if only to identify and separate dynamically active regions. One primary issue with
single-trajectory metrics is that they are not frame-indifferent. That is, they depend on the reference frame of the observer.
One may argue that it is sufficient to require all computations to be performed in the same reference frame, but the material
140   response (e.g. ridging, fracturing) of a continuum being independent of the observer is one of the main axioms of mechanics
(Gurtin, 1981). Frame-indifference is, therefore, a foundational benchmark that diagnostics must meet in order to identify
coherent features in any deforming continuum. The rate of strain tensor is a frame-indifferent tensor, but the deformation,
divergence, and shear metrics as defined above, are not objective, and depend on the reference-frame of the user. In Appendix
A3, we provide a simple example of this lack of self-consistency. As mentioned before, in slowly-varying frames, TSEs are
145   quasi-objective, approximating objective tangential stretching with errors bounded by the temporal derivative of the velocity
field.

We exhibit the utility of TSE and $\overline{\text{TSE}}$ spatio-temporal analysis for two experimental sea ice buoy data sets, the N-ICE2015
(Itkin et al., 2015, 2017) and MOSAiC expeditions (Krumpen et al., 2020), and data from the International Arctic Buoy Program
(IABP) (International Arctic Buoy Programme, 2022). The six-month Norwegian Young sea ice cruise (N-ICE2015) sought to
150   understand the rapid shift to younger and thinner sea ice, and its effect on energy fluxes, sea ice dynamics, ecosystems, in the
Arctic basin. Numerous in-depth studies have evaluated the thin ice and weather conditions during the N-ICE2015 experiment
(e.g. Cohen et al., 2017; Granskog et al., 2017; Itkin et al., 2017; Graham et al., 2019a). Itkin et al. (2017) conducted a thorough
investigation of the ice response to N-ICE2015 storms, as identified by Cohen et al. (2017), which provides a test bed of buoy
data where atmosphere-ice relationships during brief synoptic events are well understood.
155   The Multidisciplinary drifting Observatory for the Study of Arctic Climate (MOSAiC), was the largest multidisciplinary
Arctic expedition to date and centered around the research icebreaker Polarstern (Knust, 2017; Nicolaus et al., 2022; Rabe et al.,
2022) which was moored to an ice floe for an entire year (Krumpen et al., 2020). MOSAiC provides an unprecedented look at
winter ice dynamics with 213 unique GPS-tracked buoys and complementary atmosphere, ocean, ecology and biogeochemistry
data. Though MOSAiC analysis is now just beginning, a deeper storm-by-storm analysis of the MOSAiC events will follow, as
160   will a more thorough analysis of MOSAiC buoys with the contour integral approach. As there is currently limited mid-winter
buoy data available for the Arctic, these two experimental datasets provide the best testbed for evaluating the efficacy of TSEs
to identify significant stretching events at high spatial resolution in coherent ice floes. IABP data were also evaluated as they
have been a useful ground-truth of sea ice motion for several decades, and continue to provide invaluable information for both
model verification and understanding the complexities of ice dynamics, though at a significantly larger spatial scale (Rampal
165   et al., 2009; Bouchat and Tremblay, 2020).

3 Results

Results here focus on the ability of TSEs to localize temporal and spatial regions with significant stretching, and subsequent fracturing, during short-lived mid-winter storms. Cohen et al. (2017) found winter storms north of Svalbard during N-ICE2015 to have durations between 3 and 10 days. We thus calculate TSE over three day periods so as to capture the storm-scale Lagrangian stretching. This balances a high temporal resolution of material stretching while dampening influences of measurement noise and sub-daily oscillations. The temporal resolution of TSE calculations are only limited by the signal-to-noise ratio for GPS trajectory data, with shorter integration times likely affected more significantly by the noise. The instantaneous limit of the TSEs are also well-defined and provide approximations of hyperbolic (or parabolic) objective Eulerian coherent structures, which are the instantaneous limits of hyperbolic (or parabolic) LCSs (Serra and Haller, 2016).

As the stretching exponents are Lagrangian diagnostics, the stretching exponent time series are calculated over a three-day forward-looking window, at each time t. In this way, large TSE and $\overline{\text{TSE}}$ values should precede significant storms and breakup events, and will be slightly out of phase with Eulerian polygon-based divergence, shear, and deformation time series. Indeed, we find this phase difference is on the order of the length of the integration window when maximizing the cross-correlation between TSEs and div and D. We verify here how TSE can identify significant ice dynamics events using three different data sources at different spatial scales: synoptic storm analysis from a targeted experiment, LKF formation in subsequent SAR frames on the order of tens of kilometers, and sea ice brightness temperature measurements that show fractures at scales of hundreds of kilometers.

3.1 N-ICE2015

The N-ICE2015 experiment focused on the effects of the recent rapid shift to younger and thinner ice north of Svalbard, with two separate buoy deployments from January to mid-March, and late April to June, 2015. For our analysis, 24 buoy trajectories were cleaned in the same manner as in Itkin et al. (2017), and resampled at a 1 hr^{-1} frequency using a linear interpolant. As we calculate TSE from single trajectories, we did not select single representative buoys from close clusters, but calculated stretching exponents for every buoy available.

The winter deployment of buoys for the N-ICE2015 campaign was hindered by logistical challenges as the researchers deployed buoys in the polar night by snow machines and on skis. This resulted in an initially quasi-linear buoy array geometry, with many of the triangles formed by buoy vertices having small angles ($< 15°$) and thus providing unreliable calculations of divergence, shear, and deformation (Itkin et al., 2017). Upon removing the most unreliable calculations, Itkin et al. (2017) successfully showed the impact of storms, as identified by Cohen et al. (2017), on polygon-based shear, divergence and deformation signatures during the winter and spring deployments.

The significant N-ICE2015 storms from Cohen et al. (2017), are shaded as pink regions in Figure 1, overlaying TSE and $\overline{\text{TSE}}$ values for all buoys in the two deployments. In winter, every storm of note was preceded by a TSE extrema, including the short 10-hour storm on Jan 22, and the 5-hour storm on Feb 13. As well, every coherent TSE peak above $1d^{-1}$ was immediately followed by a significant storm in the TSE integration window. This is in contrast to Itkin et al. (2017) who calculated a

significant divergence and shearing event for the buoy array on January 26 that did not correspond with the presence of a
storm, but was instead related to a change in wind-direction. TSE and $\overline{\text{TSE}}$ values in Fig. 1a-b do not reveal such a coherent
divergence or deformation event, thus indicating a possible advantage of using single-buoy material stretching where there is
less reliance on buoy array geometry.

Storms during the spring deployment also coincided with significant stretching events, even for the sub-12-hour storms on
May 16, May 30, and June 8. Similar to the analysis of Itkin et al. (2017), stretching time series for the spring deployment ex-
hibited sub-daily oscillations, likely related to a more broken sea ice cover, tides, or inertial motions. There is also significantly
more noise in the winter and spring time series when compared with the MOSAiC data (below), which we found is actually an
effect from the noise in the underlying GPS measurements. Due to this, $\overline{\text{TSE}}$ is less informative as small fluctuations have a
positive cumulative effect during summation.

3.2 MOSAiC

MOSAiC was the largest multidisciplinary Arctic expedition to date, spanning the winter of 2019-2020 (Krumpen et al., 2020).
213 unique GPS-tracked buoys were deployed around the research icebreaker Polarstern and migrated through the transpolar
drift. We focus here on the paths of 101 buoys originating in close proximity to Polarstern. In Figure 2a-d we compare time
series of TSE and $\overline{\text{TSE}}$ with instantaneous approximations of divergence and deformation. We plot all 101 TSE time series
as there is an impressive coherence in stretching exhibited by the entire cluster, with local rates of deformation varying most
during peak stretching events. This allows us to analyze both the temporal localization of sea ice fracture by TSE, as well as
relate spatial differences of trajectory stretching to nearby LKFs.

Triads were also handpicked from the MOSAiC buoys with data spanning October 2019 to June 2020. The arrays were
selected to maintain reasonable shapes (no small angles, area greater than 1km^2) from the beginning to the end of the time
series. This was performed in order to avoid oversampling with a tesselation of triangles, but does require user discretion. A
deeper comparison and refinement of geometrically suitable arrays in the MOSAiC data is a current topic of research. In Figure
2b and 2d, blue dots indicate the instantaneous value from each triad, and the black lines show the mean over all triangles.

Qualitatively, prior to the January 31 event, there is a reasonable agreement between TSE and triad-based events, when
accounting for the three-day integration window. For the entire period, one finds that all strong divergence and deformation
events are accounted for as extrema in the TSEs, though often with a different relative magnitude. One such example is the local
maximum around January 14 in div and D that is much more extreme in TSE and $\overline{\text{TSE}}$. The div mean provides a suggestion
of whether divergence or convergence was more prevalent amongst the triads at a given time, but the significant scatter of both
positive and negative values obscures such behavior at finer spatial scales. In contrast, there is much less ambiguity of the
characteristic ice behavior for the entire cluster in the TSE series suggesting the cluster remained part of a largely coherent
structure, with variance between buoys appearing during dynamic events.

After January 31, several relatively large peaks in TSE appear as minor oscillations in div or D, or are not present. This
indicates local dynamic stretching and potential fracture events may not be evident with the contour integral metrics. One such
example is shown for the peak on April 17 highlighted by the vertical black dashed line. In div and D plots, we also show
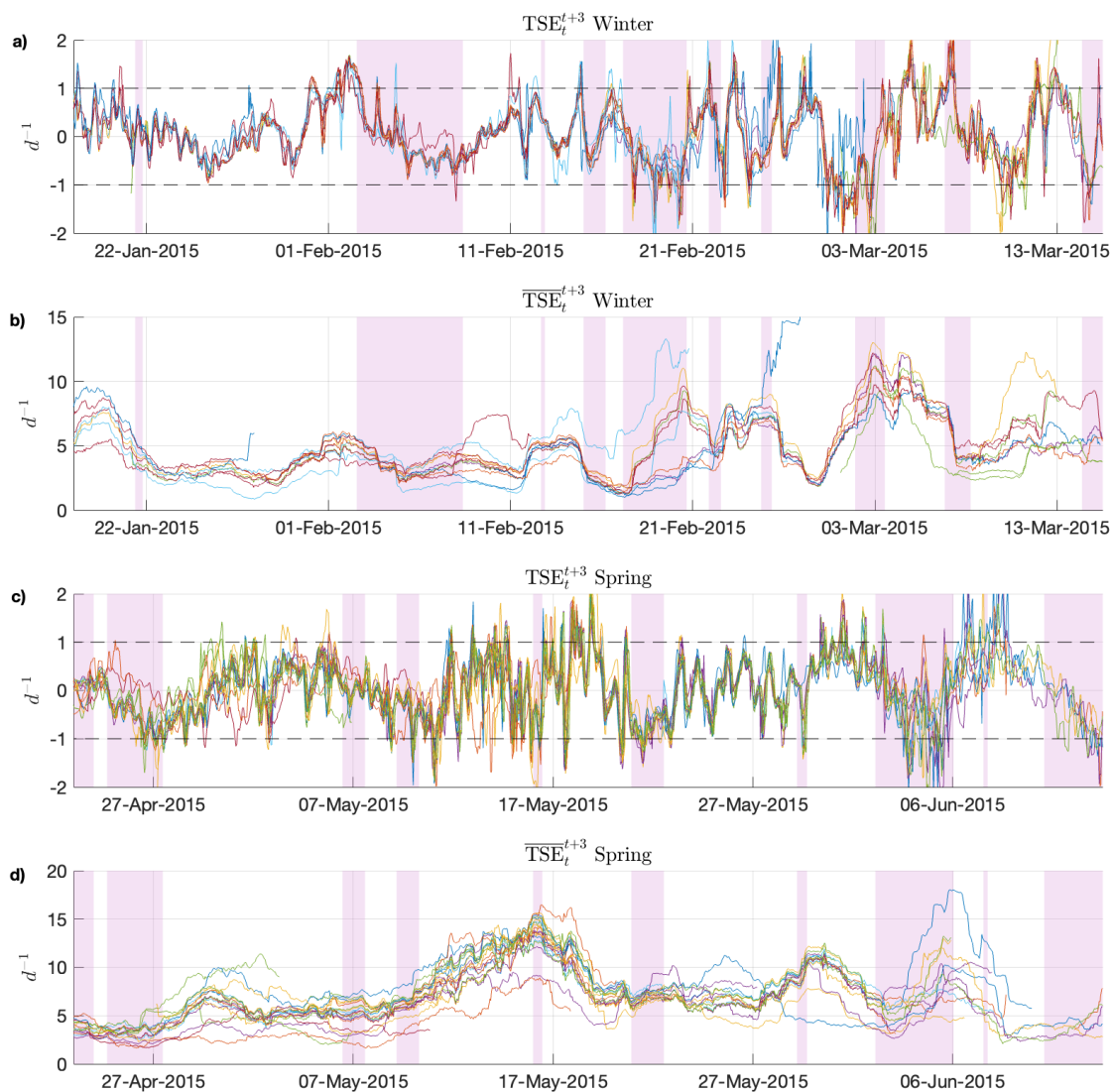
Figure 1. Comparison of TSE and $\overline{\mathrm{TSE}}$ time series during the N-ICE2015 experiment. A good correlation between strong stretching events and influential Arctic storms is shown as TSE extrema precede all storms and show no false positive sea ice stretching indicators.

the 3-day integration window in green. This example was chosen due to the concurrent availability of pre- and post-storm SAR data during the period after the major January 31 event, as well as a relatively minor signature in div and D. The large

235 stretching indicated by TSE on April 17, corresponds with multiple leads that formed throughout the domain of the MOASiC buoys. These fractures can be seen in the pair of HH polarization Sentinel-1 frames (Copernicus, 2020) (Fig. 2e-f), where white regions indicate new ice forming in leads or wind-driven waves (Grenfell et al., 1998). Points showing buoy locations have been colored by the April 17 TSE values. The spatial distribution of TSE values is difficult to interpret, and would require a deeper analysis of the meteorological and ice conditions.

240   In the 3-day window following the Apr 17 TSE and $\overline{\text{TSE}}$ peak, the average buoy divergence oscillated around zero, with the magnitude staying below $0.1d^{-1}$. The contribution to total deformation from shear was slightly larger, with a peak mean deformation of $0.46d^{-1}$ at 17:00, April 17. The choice of triangles dictates which LKF are spanned during this dynamic event, and may explain why there was a weak deformation signature from the triads. As well, the lack of objectivity or trapezoid rule errors when using Green's theorem approximations with triads, as detailed in Appendix A2, may also contribute. In this

245 scenario, the stretching and relaxation measured by TSE presents a clear correlation with material deformation of the ice and suggests TSE may provide ice behavior insight during previously neglected periods.

    Note, further user refinement may also provide buoy arrays that are geometrically more suitable for the Green's theorem calculations and provide more accurate spatial velocity gradients approximations, as there is currently no automated best practice.

250 **3.3 IABP**

The international arctic buoy program is a network of drifting buoys in the Arctic ocean dating back to the 1970's. In comparison with the previous two experiments, IABP buoy density is significantly lower, but the length of the IABP buoy record and its considerable spatial coverage allows for analysis of ice dynamics at much greater scales. In this section, we focus specifically on behavior in the Beaufort sea from October 2016 to October 2017. During this winter, thinner than usual sea ice may have

255 caused the collapse of a typical high-pressure system over the Beaufort and anomalous surface winds (Moore et al., 2018).

    We resampled the L2 IABP buoy data (https://iabp.apl.uw.edu) to a 6-hour sampling, using a linear interpolant. In Figure 3a, we show the three-day TSE for each buoy in the Beaufort during that period in grey. The maximum distance between buoys sampled here is approximately 30 times the lengthscale of the previous experiments. Due to the sparse sampling over a much larger spatial domain, there is much more variance around the mean TSE value, shown in black. The peak mean TSE value

260 during this period is indicated by a red dots, signifying a period of maximal stretching and deformation over a large domain. The following two peaks are also identified by red dots. These events correspond with three dynamic shifts in Beaufort sea ice structure and behavior. The frame pairs in Figure 3b-d show before and after frames of AMSR2 Sea Ice Brightness Temperature (89V GHz) (Meier et al., 2018) for times corresponding to high TSE values. Buoy positions are again colored by TSE in the initial frame and colormaps are consistent across all frames. A full animation of this breakup can be found in the supplementary

265 video.
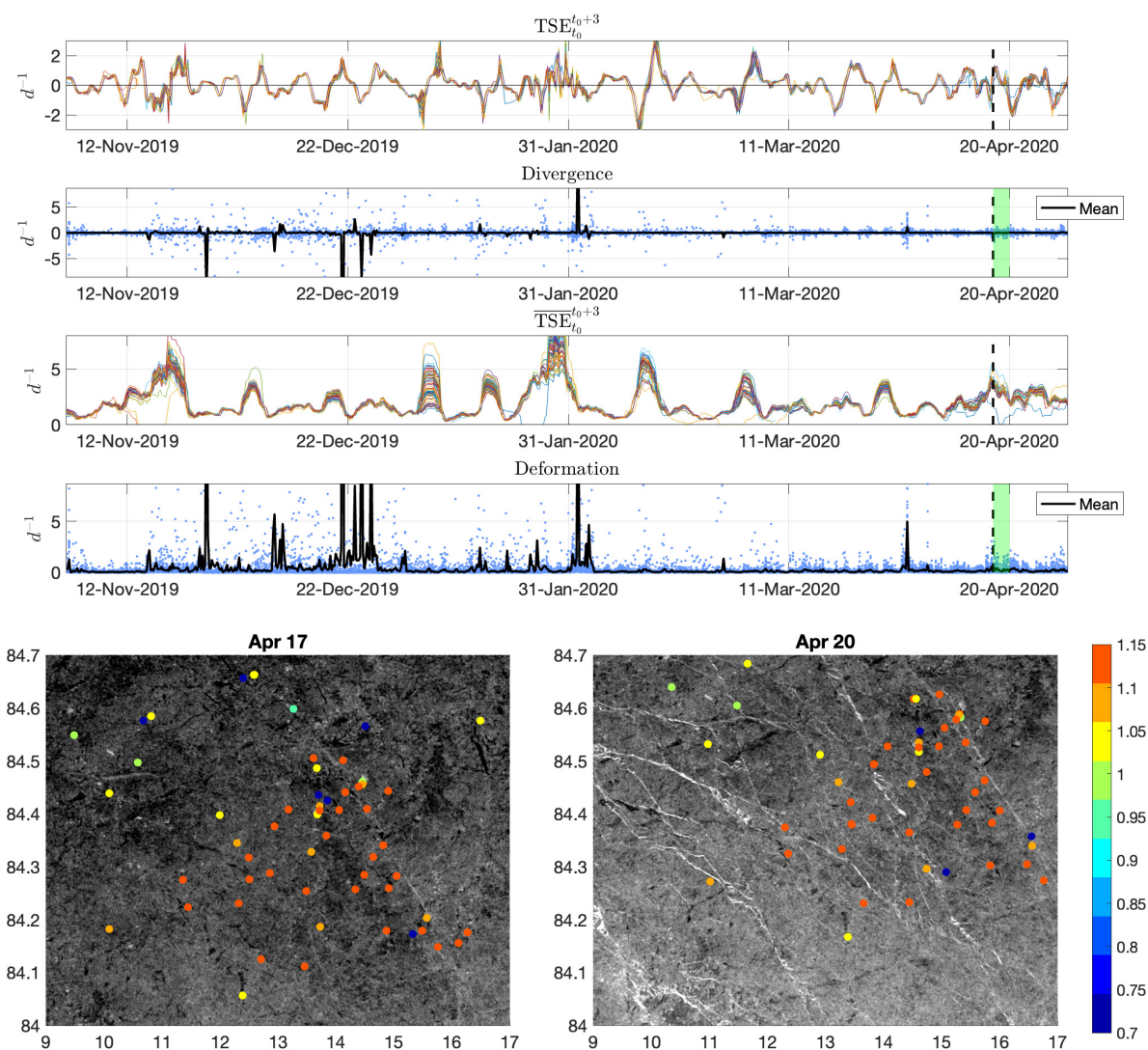
Figure 2. Time series comparison of trajectory stretching exponents and common buoy-array based approximations of divergence of and total deformation during the MOSAiC expedition. The vertical black dashed lines show a sea ice fracture event that was largely missed in the divergence and deformation. Bottom panels show a before and after comparison of HH Sentinel-1 frames, the creation of multiple LKFs in white, and the TSE values of nearby buoys during the period.

The first event corresponds to stretching from March 26 to March 29, 2017. Previous TSE peaks built up this highest TSE value, at which point an initial significant fracture formed when the sea ice detached from the landfast ice on the northern coast of Alaska. The fracture extends to just off the coast of Banks Island (BI in Figure 3c) as the ice in the Beaufort Gyre begins to freely rotate in an anticyclonic motion. All buoys in the region indicate high (red) TSE values, suggesting a distinct shift from

270 previous behavior. From April 3 to April 8, significant fracturing throughout the region south of 76° N occurred, with another major fracture extending off the northwest corner of banks island. The buoys in the region of this enhanced fracturing showed high TSE values, whereas buoys further north without new fracturing showed low TSE values. The last pair of frames show the last major shift in ice dynamics from April 13 to April 17. At this time, a major lead formed off of Prince Patrick Island (PI). This was the last stage of the changing dynamics, after which all ice south of the PI lead exhibited a much freer anticyclonic

275 rotation, decoupled with the surrounding ice. Again, the highest TSE values were found in the spatial domain where significant ice breakup was occurring, with lower TSE values, hundreds of kilometers away, delimiting the fracture domain to the North.

4   Conclusions

We find that TSEs successfully identify significant local material deformation tangent to individual sea ice buoy trajectories. Periods of strong local stretching are representative of changing ice dynamics in a neighborhood to 10-100 km. That is,

280 single-buoy trajectory stretching provides insight into much larger coherent sea ice structures, and distant fracture events. This local-regional connection provides a valuable avenue for researching sea ice dynamics in sparsely sampled regions, and understanding the changing rheology of sea ice. In contrast, conventional polygon-based approaches provide an estimate of the spatial-average divergence, shear, or deformation over a large area, with errors increasing as area decreases, number of buoys decreases or the array becomes skewed.

285 Approaching sea ice dynamics through quasi-objective stretching, we were able to predict coherent deformation events in both concentrated buoy experiments, and in large sparsely-sampled IABP data. Spatial and temporal signatures of stretching with TSE are well correlated with formation of nearby leads and changing ice transport patterns, as well as with the concurrence of well studied sea-ice-impacting storms. For two high resolution mid-winter buoy deployments, we find that the TSE had greater sensitivity to sea ice deformation than the common polygonal approach, and potentially avoided a false positive

290 identification.

Specifically, TSEs accurately predicted the onset of major storms in the N-ICE2015 experiment, and did not identify a mysterious storm-free event that was described by Itkin et al. (2017). For the first half of the MOSAiC experiment, we found a good qualitative agreement between polygon-based metrics and the TSEs, though this correlation was much weaker following a large midwinter storm. During this latter half, we verified TSEs were able to identify an influential stretching event that was

295 much less evident with Green's theorem methods. Lastly, TSEs were able to spatially and temporally isolate major fracture events during Beaufort sea ice breakup using IABP data at a much lower spatial resolution. A buildup of stress in the Beaufort sea was detailed by increasing local TSE maxima, until an initial separation formed at the land-fast ice during the seasonal TSE
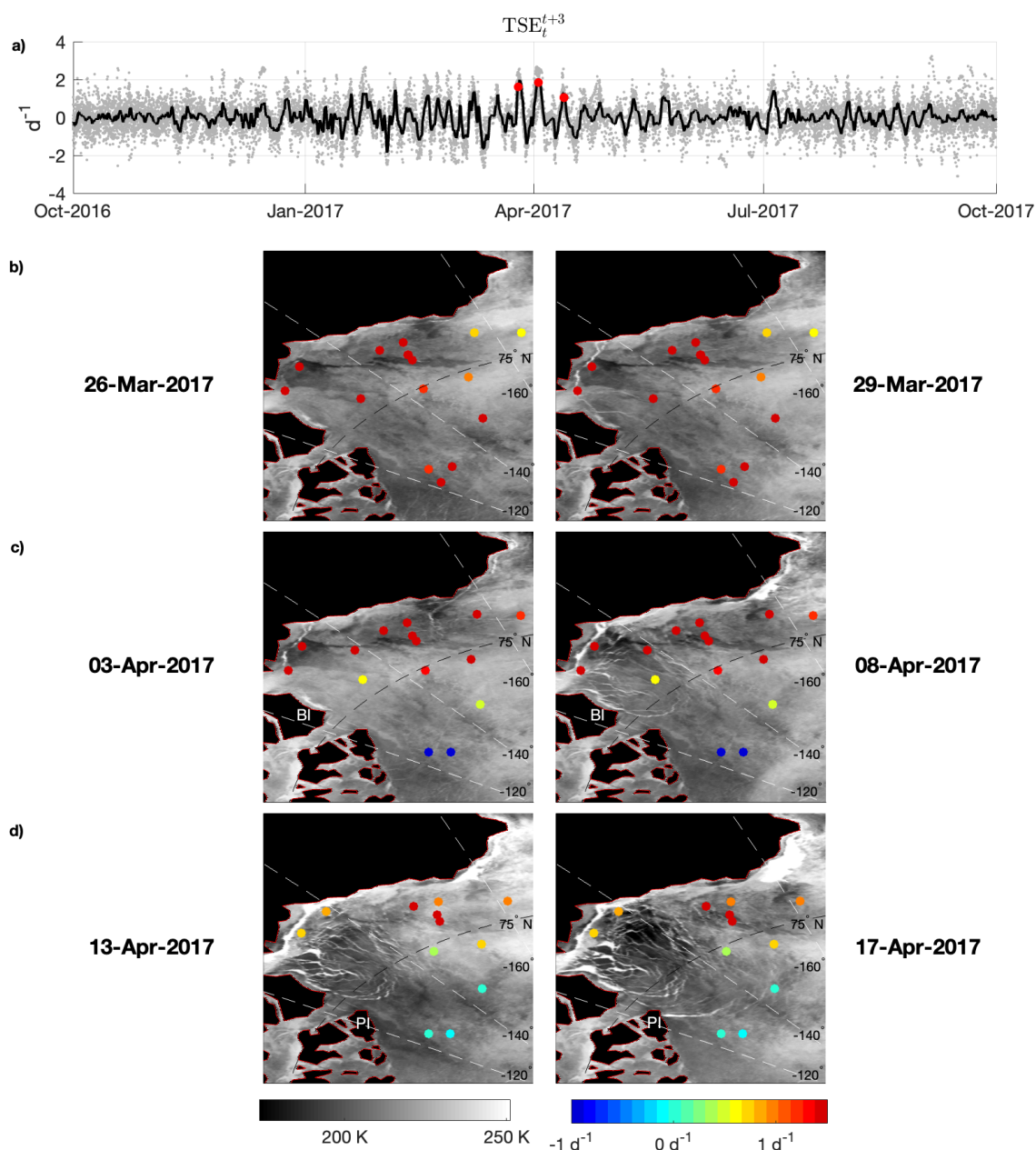
Figure 3. The three steps of the Beaufort gyre sea ice freeing itself from surrounding ice beginning its spring anticyclonic acceleration. The top time series shows TSE values for all buoys in the region, with mean shown in black. The bottom frames show sea ice brightness temperature before-and-after pairs for the three events highlighted as red dots in the time series.

peak. Subsequent diminishing peaks released the remaining stress, breaking up the ice and further detaching from land-fast regions, creating a coherent mass of rotating ice that was delimited spatially with TSE.

300   The single-buoy quasi-objective trajectory stretching exponents identify events that are potentially significant in terms of understanding atmosphere-ice-ocean exchange processes are a suitable complement to common, polygon-based divergence, shear, and deformation approximations. We find TSE usage provides some distinct advantages and potential improvements for future research:

1) TSEs identify deformation events from a single buoy and are thus unaffected by buoy array geometry, or the number of
305   buoys deployed. As buoys passively follow ice floes, we can still obtain insights into ice dynamics as arrays become heavily skewed and non-uniform. TSE maintains integrity in this situation, whereas arrays of buoys become aligned and unsuitable for strain estimates due to shearing in the ice pack. This expands the domain of potential analysis, and reduces logistical burdens of Arctic and Antarctic expeditions as stretching dynamics can be studied with TSE from linear, randomly distributed, or organized arrays.

310   2) As TSEs are quasi-objective metrics in continua, their values provide a useful proxy for frame-indifferent (objective) measures of stretching, with a quantitative difference depending on the compressibility of the ice and slowly-varying nature of the flow. In a heavily fractured ice context, the degree to which these single-trajectory metrics approximates along-trajectory ice stretching varies, but this work suggests positive correlations with remotely-sensed dynamic fracture and breakup events. Further numerical and observational experiments can help improve these correlations.

315   3) TSE values do not need to be separated or averaged based on length scales (e.g. Itkin et al., 2017), and showed great success in identifying fracture regions at a wide range of spatial scales.

4) TSE calculations are mathematically simple as TSE is calculated using only buoy speed and does not require projection to orthogonal velocity components. Speed can be calculated using geodesics between GPS locations, which prevents any inconsistencies of results due to choice of map projection or projection distortions, or needing to perform differential calculus
320   in an elliptic geometry. Furthermore, TSE is parameter-free with integration time being the only user-chosen value.

Calculating TSE from single buoy trajectories requires significantly less effort than SAR-based approaches, is not subject to the same errors (e.g. Bouchat and Tremblay, 2020), and also supplements data in the pole hole during winter (e.g. Krumpen et al., 2021). If we can further verify the slowly-varying nature of sea ice at sub-diurnal time scales, TSE may also fill in temporal gaps due to the sparse monitoring of satellites. Calculating TSE fields from more general feature trajectories, such as
325   from X-Band and HF radar or SAR datasets, would be a straight-forward application of Eq (4) & (5) and can also enrich the analysis of sea ice dynamics in existing datasets.

The ability of TSE to overcome some of the short-comings of other buoy approaches may also provide an additional source of deformation information, such as is necessary to constrain and improve sea-ice models (Bouchat and Tremblay, 2020). A modeling study of compressibility and slowly-varying impacts could be useful for TSE applications in model development,
330   as would a controlled comparison with divergence, deformation, and shear to aid the broader community in the physical interpretation TSE signals. This would help interpret TSEs as complementary sources of stretching information when buoy arrays are aligned linearly due to strong shear, have edges that span large distances encompassing multiple fractures or coherent

structures, or have areas below tolerable error thresholds. In remote polar regions where data is still difficult to obtain, but the changing climate has an outsized impact, TSEs provide new physics-based insights into ice dynamics while only requiring single GPS tracks.

Our findings suggest that spatio-temporal analysis of local and regional sea ice dynamics should be revisited with a comparison between single-trajectory and spatial velocity gradients. Our comparisons suggest potentially significant dynamic events in terms of understanding atmosphere-ice-ocean exchange processes may go undetected using conventional polygon-based methods, or in the case of N-ICE data, may be inaccurately detected. This advantage stems from the TSEs' ability to identify stretching in a small neighborhood of individual buoys and connect local changes with broader ice behavior. A deeper understanding of TSEs connection to more broadly used ice dynamics metrics will help researchers understand how TSE can inform ice responses to various forcings.

Appendix A: Introduction

The first section of the Appendix provides a verification of the assumption that sea ice is a slowly varying flow to satisfy criteria for the quasi-objectivity of TSEs. The latter sections provide two simple analytic examples of buoy motion to illuminate Green's theorem calculation responses for buoy-array diagnostics. The first example shows the lack of objectivity (frame-indifference) of shear, divergence, and deformation as defined through polygonal approximations in the main text. This proves these diagnostics are not self-consistent, even in the same experiment, and do not quantify true material responses (e.g. stretching, fracture) of sea ice. The second example shows how the Green's theorem approximation fails to predict any divergence for a triad in a simple divergent flow.

A1 Slowly-varying condition of sea ice

TSE is a quasi-objective metric, indicating it approximates an objective metric under a given condition. For the work presented here, this requires that the velocity field of interest be slowly varying. That is, $|\mathbf{v}_t(\mathbf{x}(t),t)| \ll |\mathbf{a}(t)|$, where $\mathbf{a}(t)$ is the Lagrangian velocity. In order to calculate the temporal derivative on the LHS, we rely on daily gridded sea ice velocity data from Tschudi et al. (2018) as a best estimate for the flow. While one can calculate $\mathbf{a}(t)$ from trajectory data, discrete calculations of $\mathbf{v}_t(\mathbf{x}(t),t)$ rely on repeat measurements of velocity at the same location. In this way, we require gridded velocity data to validate the slowly-varying assumption.

The use of Pathfinder sea ice displacement grids comes with its own errors, such as the spatial gradient artifacts previously identified by Szanyi et al. (2016a). Furthermore, the low temporal resolution of this data smooths the short-time variability of surrounding instantaneous shear and fracture events. Prior to the development of a more robust gridded dataset of ice velocities, this remains the best available option.

The probability function in figure A1 shows that for the majority of the Arctic domain, the slowly varying condition is satisfied pointwise along sea ice trajectories. This probability is representative of mid-winter ice conditions, and may vary

365   depend on a specific time window, the resolution of the underlying Pathfinder velocity field.

A2   Trapezoid rule errors for buoy arrays in a continuous flow

Consider the incompressible 2D flow

$$u(x,y) = -y^2, \qquad v(x,y) = x^2. \tag{A1}$$

One finds $\partial u/\partial x(x,y) = \partial v/\partial y(x,y) = 0$, and $\mathrm{div}(x,y) \equiv 0$. Consider also the equilateral triangle formed by three buoys

370   positioned on the unit circle, $(x_{b1}, y_{b1}) = (\cos(\frac{\pi}{2}), \sin(\frac{\pi}{2}))$, $(x_{b2}, y_{b2}) = (\cos(\frac{7\pi}{6}), \sin(\frac{7\pi}{6}))$, $(x_{b3}, y_{b3}) = (\cos(\frac{-\pi}{6}), \sin(\frac{-\pi}{6}))$.

We estimate the "Green's theorem divergence" for this triad as $\mathrm{div_G} = -0.5$. Though this flow is entirely divergence free, the

value of $\mathrm{div_G}$ is sensitive to the triad's rotation on the unit circle. Figure S2a shows the range of $\mathrm{div_G}$ calculated as the triad is

rotated. Depending on how the vertices are oriented, this approach will suggest either a divergent or convergent flow, with the

correct value only appearing for two specific orientations.

375   In contrast to errors that have been discussed and quantified before (.eg., Lindsay and Stern, 2003; Hutchings et al., 2012;

Dierking et al., 2020), this issue arises from the approximation of the partial derivative contour integrals by the trapezoid rule.

For a generic real-valued twice differentiable function $f(x)$ defined on the interval $[a,b] \subset \mathbb{R}$, the difference between the true

integral and trapezoid rule is bounded by (Atkinson, 1989):

$$E = -\frac{(b-a)^3}{12}f''(y) \qquad y \in [a,b]. \tag{A2}$$

380   That is, the potential error of each partial derivative scales with the cube of the distance between buoys and the second derivative

of the associated velocity component along that interval. If we increase the number of uniformly distributed buoys on the unit

circle in this velocity field, we find the average divergence approximation inside the polygons quickly converges to the true

value (Figure S2b). In fact, using a four sided polygon can significantly reduce the error for this simple flow, as an equal

number of buoys can be positioned on either side of the axis dominant flow structure (Figure S2c). This improvement can be

385   expected for other flows as well, though more complex flow structures would require a greater number of vertices to avoid

these same errors. Analogous errors are evident in Green's theorem approximations of shear and total deformation as well,

reminding researchers to consider the number of buoys and methods used when quantifying sea ice dynamics.

A3   Frame-indifference violation

Assume you have GPS trajectory data for two buoys (b_1 and b_2) deployed nearby a research vessel (s_1), all of which are

390   anchored to the surrounding ice (see Figure S1). For simplicity, assume the vessel is positioned at $(x_{s1}, y_{s1}) = (0,1)$ in the

Cartesian plane, with the buoys positioned at $(x_{b1}, y_{b1}) = (-1,0)$ and $(x_{b2}, y_{b2}) = (1,0)$. Furthermore, at time t_0, assume the

velocities are steady $(u_{s1}, v_{s1}) = (0,1)$, $(u_{b1}, v_{b1}) = (-1,-1)$, $(u_{b2}, v_{b2}) = (1,-1)$, and the triangle formed by the three points

is expanding. In the given reference frame, such as from a satellite, using the polygon-based approximation of Green's theorem,
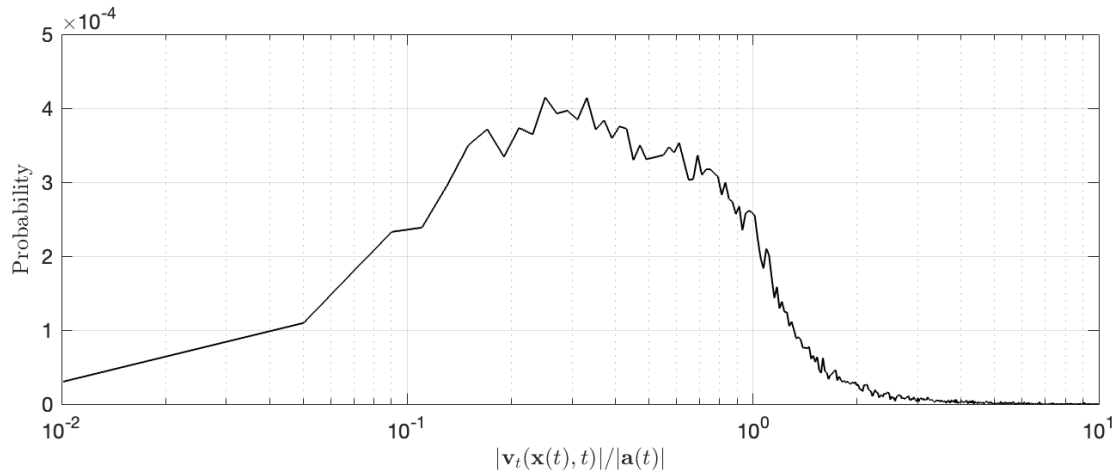
Figure A1. Example verification of assumption of Arctic sea ice as slowly varying from Polar Pathfinder Daily 25 km EASE-Grid Sea Ice Motion Vectors, Version 4. $|\mathbf{v}_t(\mathbf{x}(t), t)|/|\mathbf{a}(t)|$ calculated from 50-day sea ice trajectories in 2017.
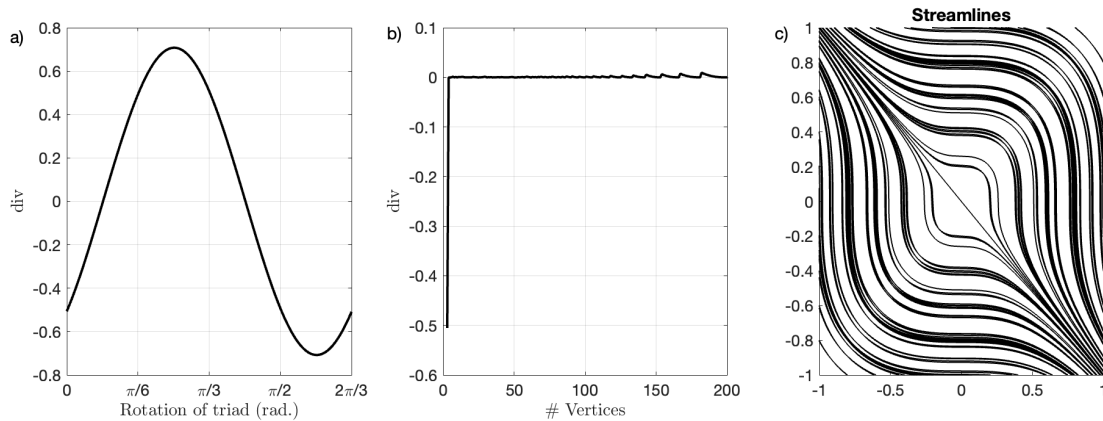
Figure A2. a: Average divergence as approximated by unit equilateral triad for all possible rotations. b: Average divergence as approximated by unit polygons as a function of the number of vertices used in the approximation. c: Streamlines for the flow in (A1)

one calculates the following $\mathrm{div} = 3t^{-1}$, $\mathrm{shr} = 1t^{-1}$, and $D = 3.2t^{-1}$, where t is a unit of time. For a reference frame moving
395 with the research vessel, such as one would measure from an on-board radar tracking ice features (e.g., Lund et al., 2018), the relative distance and speeds between the three objects would not change, but, in the reference-frame of the ship, the velocities are now $(\tilde{u}_{s1}, \tilde{v}_{s1}) = (0,0)$, $(\tilde{u}_{b1}, \tilde{v}_{b1}) = (-1,-2)$, $(\tilde{u}_{b2}, \tilde{v}_{b2}) = (1,-2)$. From the position of the on-board radar, we would now calculate $\mathrm{div} = 7t^{-1}$, $\mathrm{shr} = 5t^{-1}$, and $D = 8.6t^{-1}$.
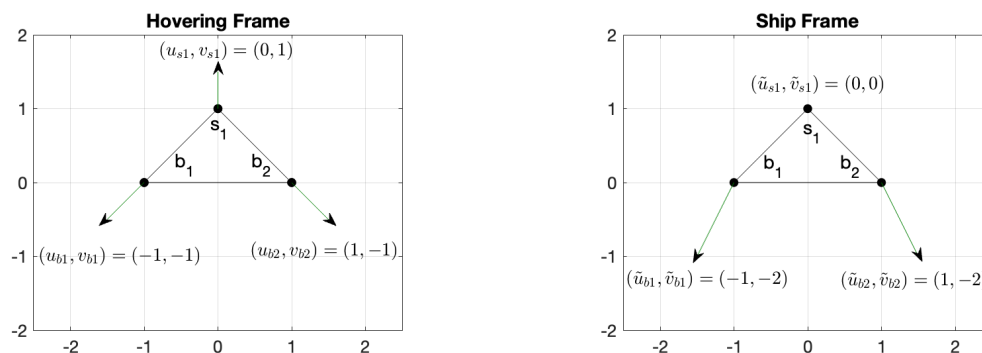
Figure A3. Graphical representation of the two reference frames and object velocities, discussed in A3

Code availability. MATLAB scripts for calculating trajectory stretching exponents can be found here: https://github.com/NikAksamit/TRA_
TSE

Data availability. The MOSAiC drifter data (Bliss et al., 2021) from the research platform POLARSTERN (Knust, 2017) is available here:
https://arcticdata.io/catalog/view/doi:10.18739/A2Q52FD8S, the N-ICE2015 data (Itkin et al., 2015) is available here: https://doi.org/10.
21334/npolar.2015.6ed9a8ca, the IABP data (International Arctic Buoy Programme, 2022) is available here: http://iabp.apl.uw.edu/data.html,
the AMSR data (Meier et al., 2018) is available here: https://doi.org/10.5067/NX1R09ORNOZN, and the Sentinel-1 data (Copernicus, 2020)
is available here: https://asf.alaska.edu/data-sets/sar-data-sets/sentinel-1/.

Video supplement. The supplemental video provides a NASA Worldview animation of the Beaufort Sea ice breakup detailed in Section 3.3.
The animation can be viewed at https://youtu.be/WHCsOaL4Nks

Author contributions. NA and RS designed and developed the experiment. NA developed the methods. NA and JH contributed calculations
for the analysis. All authors contributed to the analysis of the results and the writing of the manuscript.

Competing interests. The authors declare no competing interests.

Acknowledgements. The authors would like to acknowledge funding from the Swiss National Science Foundation Postdoc Mobility Fel-
lowship Project P400P2 199190 to Nikolas Aksamit, and a Natural Sciences and Engineering Research Council of Canada (NSERC) Dis-
covery Grant to Randall Scharien. Jennifer Hutchings was funded through the National Science Foundation grant 1722729. Randy might

also have MOSAiC funding to acknowledge. The authors would also like to thank Angela Bliss for preparing and providing the MOSAiC

415   buoy data, who accepts acknowledgement instead of co-authorship. Data used in this manuscript was produced as part of the international

Multidisciplinary drifting Observatory for the Study of the Arctic Climate (MOSAiC) with the tag MOSAiC20192020 and the Project ID:

AWI_PS122_00. We thank all those who contributed to MOSAiC and made this endeavor possible (Nixdorf et al. 2021).

References

Atkinson, K. E.: An Introduction to Numerical Analysis, John Wiley & Sons, 2nd edition edn., 1989.

Bliss, A., Hutchings, J., Anderson, P., Anhaus, P., Belter, H. J., and et al.: Sea ice drift tracks from the Distributed Network of autonomous buoys deployed during the Multidisciplinary drifting Observatory for the Study of Arctic Climate (MOSAiC) expedition 2019 - 2021, (Arctic Data Center), https://doi.org/doi:10.18739/A2Q52FD8S, 2021.

Bouchat, A. and Tremblay, B.: Reassessing the Quality of Sea-Ice Deformation Estimates Derived From the RADARSAT Geophysical Processor System and Its Impact on the Spatiotemporal Scaling Statistics, Journal of Geophysical Research: Oceans, 125, 1–29, https://doi.org/10.1029/2019JC015944, 2020.

Cohen, L., Hudson, S. R., Walden, V. P., Graham, R. M., and Granskog, M. A.: Meteorological conditions in a thinner Arctic sea ice regime from winter to summer during the Norwegian Young sea ice expedition (N-ICE2015), Journal of Geophysical Research, 122, 7235–7259, https://doi.org/10.1002/2016JD026034, 2017.

Copernicus: Sentinel data 2020. Retrieved from ASF DAAC 17 March, 2022, processed by ESA, https://doi.org/10.21334/npolar.2015.6ed9a8ca, 2020.

Dierking, W., Stern, H. L., and Hutchings, J. K.: Estimating statistical errors in retrievals of ice velocity and deformation parameters from satellite images and buoy arrays, Cryosphere, 14, 2999–3016, https://doi.org/10.5194/tc-14-2999-2020, 2020.

Graham, R. M., Cohen, L., Ritzhaupt, N., Segger, B., Graversen, R. G., Rinke, A., Walden, V. P., Granskog, M. A., and Hudson, S. R.: Evaluation of six atmospheric reanalyses over Arctic sea ice from winter to early summer, Journal of Climate, 32, 4121–4143, https://doi.org/10.1175/JCLI-D-18-0643.1, 2019a.

Graham, R. M., Itkin, P., Meyer, A., Sundfjord, A., Spreen, G., Smedsrud, L. H., Liston, G. E., Cheng, B., Cohen, L., Divine, D., Fer, I., Fransson, A., Gerland, S., Haapala, J., Hudson, S. R., Johansson, A. M., King, J., Merkouriadi, I., Peterson, A. K., Provost, C., Randelhoff, A., Rinke, A., Rösel, A., Sennéchael, N., Walden, V. P., Duarte, P., Assmy, P., Steen, H., and Granskog, M. A.: Winter storms accelerate the demise of sea ice in the Atlantic sector of the Arctic Ocean, Scientific Reports, 9, 1–16, https://doi.org/10.1038/s41598-019-45574-5, 2019b.

Granskog, M. A., Rösel, A., Dodd, P. A., Divine, D., Gerland, S., Martma, T., and Melanie J. Leng: Snow contribution to first-year and second-year Arctic sea ice mass balance north of Svalbard, Journal of Geophysical Research: Oceans, 122, 1–22, https://doi.org/10.1002/2016JC012398.Received, 2017.

Grenfell, T. C., Barber, D. G., Fung, A. K., Gow, A. J., Jezek, K. C., Knapp, E. J., Nghiem, S. V., Onstott, R. G., Perovich, D. K., Roesler, C. S., Swift, C. T., and Tanis, F.: Evolution of electromagnetic signatures of sea ice from initial formation to the establishment of thick first-year ice, IEEE Transactions on Geoscience and Remote Sensing, 36, 1642–1654, https://doi.org/10.1109/36.718636, 1998.

Gurtin, M. E.: An Introduction to Continuum Mechanics, Academic Press, San Diego, USA, 1st edn., 1981.

Haller, G.: Lagrangian Coherent Structures, Annual review of fluid mechanics, pp. 137–162, https://doi.org/10.1002/9783527639748.ch3, 2015.

Haller, G. and Yuan, G.: Lagrangian coherent structures and mixing in two-dimensional turbulence, Phys. D Nonlinear Phenom., 147, 352–370, https://doi.org/10.1016/S0167-2789(00)00142-1, 2000.

Haller, G., Aksamit, N. O., and Bartos, A. P. E.: Quasi-Objective Coherent Structure Diagnostics from Single Trajectories, Chaos, 31, 043 131–1–17, https://doi.org/10.1063/5.0044151, 2021.

Haller, G., Aksamit, N., and Encinas-Bartos, A. P.: Erratum:"Quasi-objective coherent structure diagnostics from single trajectories" [Chaos
31, 043131 (2021)], Chaos, 32, 059 901, https://doi.org/10.1063/5.0090124, 2022.

Hutchings, J. K., Roberts, A., Geiger, C. A., and Richter-Menge, J.: Spatial and temporal characterization of sea-ice deformation, Annals of
Glaciology, 52, 360–368, https://doi.org/10.3189/172756411795931769, 2011.

Hutchings, J. K., Heil, P., Steer, A., and Hibler, W. D.: Subsynoptic scale spatial variability of sea ice deformation in the western Weddell
Sea during early summer, Journal of Geophysical Research: Oceans, 117, https://doi.org/10.1029/2011JC006961, 2012.

International Arctic Buoy Programme: International Arctic Buoy Programme, digital media, available at:
http://iabp.apl.washington.edu/index.html (last access: March 2022), 2022.

Itkin, P., Spreen, G., Cheng, B., Doble, M., Gerland, S., and Granskog, M. A. . . . Helgeland, C.: N-ICE2015 buoy data. Norwegian Polar
Institute., https://doi.org/10.21334/npolar.2015.6ed9a8ca, 2015.

Itkin, P., Haapala, J., Spreen, G., Cheng, B., Doble, M., Girard-Arduin, F., Hughes, N., Kaleschke, L., Nicolaus, M., and Wilkinson, J.: Thin
ice and storms: Sea ice deformation from buoy arrays deployed during N-ICE2015, Journal of Geophysical Research: Oceans, 122, 1–22,
https://doi.org/10.1002/2016JC012403.Received, 2017.

Knust, R.: Polar Research and Supply Vessel POLARSTERN operated by the Alfred-Wegener-Institute, Journal of large-scale research
facilities JLSRF, 3, 1–8, https://doi.org/10.17815/jlsrf-3-163, 2017.

Krumpen, T., Birrien, F., Kauker, F., Rackow, T., Von Albedyll, L., Angelopoulos, M., Jakob Belter, H., Bessonov, V., Damm, E., Dethloff, K.,
Haapala, J., Haas, C., Harris, C., Hendricks, S., Hoelemann, J., Hoppmann, M., Kaleschke, L., Karcher, M., Kolabutin, N., Lei, R., Lenz,
J., Morgenstern, A., Nicolaus, M., Nixdorf, U., Petrovsky, T., Rabe, B., Rabenstein, L., Rex, M., Ricker, R., Rohde, J., Shimanchuk, E.,
Singha, S., Smolyanitsky, V., Sokolov, V., Stanton, T., Timofeeva, A., Tsamados, M., and Watkins, D.: The MOSAiC ice floe: Sediment-
laden survivor from the Siberian shelf, Cryosphere, 14, 2173–2187, https://doi.org/10.5194/tc-14-2173-2020, 2020.

Krumpen, T., Von Albedyll, L., Goessling, H. F., Hendricks, S., Juhls, B., Spreen, G., Willmes, S., Belter, H. J., Dethloff, K., Haas, C.,
Kaleschke, L., Katlein, C., Tian-Kunze, X., Ricker, R., Rostosky, P., Rückert, J., Singha, S., and Sokolova, J.: MOSAiC drift expedi-
tion from October 2019 to July 2020: Sea ice conditions from space and comparison with previous years, Cryosphere, 15, 3897–3920,
https://doi.org/10.5194/tc-15-3897-2021, 2021.

Kwok, R. and Rothrock, D. A.: Decline in Arctic sea ice thickness from submarine and ICESat records: 1958-2008, Geophysical Research
Letters, 36, 1–5, https://doi.org/10.1029/2009GL039035, 2009.

Kwok, R., Curlander, J. C., Pang, S. S., and Mcconnell, R.: An Ice-Motion Tracking System at the Alaska SAR Facility, IEEE Journal of
Oceanic Engineering, 15, 44–54, https://doi.org/10.1109/48.46835, 1990.

Lindsay, R. W. and Stern, H. L.: The RADARSAT Geophysical Processor System: Quality of sea ice trajectory and de-
formation estimates, Journal of Atmospheric and Oceanic Technology, 20, 1333–1347, https://doi.org/10.1175/1520-
0426(2003)020<1333:TRGPSQ>2.0.CO;2, 2003.

Lukovich, J. V., Bélanger, C., Barber, D. G., and Gratton, Y.: On coherent ice drift features in the southern Beaufort sea, Deep-Sea Research
Part I: Oceanographic Research Papers, 92, 56–74, https://doi.org/10.1016/j.dsr.2014.05.013, 2014.

Lukovich, J. V., Hutchings, J. K., and Barber, D. G.: On sea-ice dynamical regimes in the Arctic ocean, Annals of Glaciology, 56, 323–331,
https://doi.org/10.3189/2015AoG69A606, 2015.

Lukovich, J. V., Stroeve, J. C., Crawford, A., Hamilton, L., Tsamados, M., Heorton, H., and Massonnet, F.: Summer extreme cyclone impacts
on arctic sea ice, Journal of Climate, 34, 4817–4834, https://doi.org/10.1175/JCLI-D-19-0925.1, 2021.

Lund, B., Graber, H. C., Persson, P. O., Smith, M., Doble, M., Thomson, J., and Wadhams, P.: Arctic Sea Ice Drift Measured by Shipboard Marine Radar, Journal of Geophysical Research: Oceans, 123, 4298–4321, https://doi.org/10.1029/2018JC013769, 2018.

Meier, W. N., Comiso, J. C., and Markus, T.: AMSR-E/AMSR2 Unified L3 Daily 6.25 km Polar Gridded 89 GHz Brightness Temperatures, Version 1., https://doi.org/https://doi.org/10.5067/NX1R09ORNOZN, 2018.

495 Moore, G. W., Schweiger, A., Zhang, J., and Steele, M.: Collapse of the 2017 Winter Beaufort High: A Response to Thinning Sea Ice?, Geophysical Research Letters, 45, 2860–2869, https://doi.org/10.1002/2017GL076446, 2018.

Nicolaus, M., Perovich, D. K., Spreen, G., Granskog, M. A., von Albedyll, L., Angelopoulos, M., Anhaus, P., Arndt, S., Jakob Belter, H., Bessonov, V., Birnbaum, G., Brauchle, J., Calmer, R., Cardellach, E., Cheng, B., Clemens-Sewall, D., Dadic, R., Damm, E., de Boer, G., Demir, O., Dethloff, K., Divine, D. V., Fong, A. A., Fons, S., Frey, M. M., Fuchs, N., Gabarró, C., Gerland, S., Goessling, H. F., Gradinger,
500 R., Haapala, J., Haas, C., Hamilton, J., Hannula, H. R., Hendricks, S., Herber, A., Heuzé, C., Hoppmann, M., Høyland, K. V., Huntemann, M., Hutchings, J. K., Hwang, B., Itkin, P., Jacobi, H. W., Jaggi, M., Jutila, A., Kaleschke, L., Katlein, C., Kolabutin, N., Krampe, D., Kristensen, S. S., Krumpen, T., Kurtz, N., Lampert, A., Lange, B. A., Lei, R., Light, B., Linhardt, F., Liston, G. E., Loose, B., Macfarlane, A. R., Mahmud, M., Matero, I. O., Maus, S., Morgenstern, A., Naderpour, R., Nandan, V., Niubom, A., Oggier, M., Oppelt, N., Pätzold, F., Perron, C., Petrovsky, T., Pirazzini, R., Polashenski, C., Rabe, B., Raphael, I. A., Regnery, J., Rex, M., Ricker, R., Riemann-Campe,
505 K., Rinke, A., Rohde, J., Salganik, E., Scharien, R. K., Schiller, M., Schneebeli, M., Semmling, M., Shimanchuk, E., Shupe, M. D., Smith, M. M., Smolyanitsky, V., Sokolov, V., Stanton, T., Stroeve, J., Thielke, L., Timofeeva, A., Tonboe, R. T., Tavri, A., Tsamados, M., Wagner, D. N., Watkins, D., Webster, M., and Wendisch, M.: Overview of the MOSAiC expedition: Snow and sea ice, Elem Sci Anth, 10, https://doi.org/10.1525/elementa.2021.000046, 2022.

Ott, W. and Yorke, J. A.: When Lyapunov exponents fail to exist, Physical Review E - Statistical, Nonlinear, and Soft Matter Physics, 78,
510 1–6, https://doi.org/10.1103/PhysRevE.78.056203, 2008.

Rabe, B., Heuze, C., Regnery, J., Aksenov, Y., Allerholt, J., Athanase, M., and Bai, Youcheng ... Zhu, J.: Overview of the MOSAiC expedition : Physical oceanography, Elem Sci Anth, 10, 1–31, https://doi.org/10.1525/elementa.2021.00062, 2022.

Rampal, P., Weiss, J., Marsan, D., and Bourgoin, M.: Arctic sea ice velocity field: General circulation and turbulent-like fluctuations, Journal of Geophysical Research: Oceans, 114, 1–17, https://doi.org/10.1029/2008JC005227, 2009.

515 Rothrock, D. A., Yu, Y., and Maykut, G. A.: Thinning of the Arctic Sea-Ice cover, Geophysical Research Letters, 26, 3469–3472, https://doi.org/10.1029/1999GL010863, 1999.

Serra, M. and Haller, G.: Objective eulerian coherent structures, Chaos, 26, https://doi.org/10.1063/1.4951720, 2016.

Serreze, M. C. and Francis, J. A.: The arctic amplification debate, Climatic Change, 76, 241–264, https://doi.org/10.1007/s10584-005-9017-y, 2006.

520 Siew, P. Y. F., Li, C., Sobolowski, S. P., and King, M. P.: Intermittency of Arctic–mid-latitude teleconnections: stratospheric pathway between autumn sea ice and the winter North Atlantic Oscillation, Weather and Climate Dynamics, 1, 261–275, https://doi.org/10.5194/wcd-1-261-2020, 2020.

Szanyi, S., Lukovich, J. V., and Barber, D. G.: Lagrangian analysis of sea-ice dynamics in the Arctic Ocean, Polar Research, 35, https://doi.org/10.3402/polar.v35.30778, 2016a.

525 Szanyi, S., Lukovich, J. V., Barber, D. G., and Haller, G.: Persistent artifacts in the NSIDC ice motion data set and their implications for analysis, Geophysical Research Letters, 43, 10,800–10,807, https://doi.org/10.1002/2016GL069799, 2016b.

Tschudi, M., Meier, W. N., Stewart, J. S., Fowler, C., and Maslanik, J.: Polar Pathfinder Daily 25 km EASE-Grid Sea Ice Motion Vectors, Version 4. Accessed: March 3, 2022., https://doi.org/https://doi.org/10.5067/INAWUWO7QH7B, 2018.